In situ measurement of plasticity accompanying Hydrogen induced cracking

L. Stermann, G. Simon, L. Vanel, D. Tanguy

International Journal of Fracture manuscript No.
(will be inserted by the editor)

In situ measurement of plasticity accompanying Hydrogen induced cracking.

L. Stermann · G. Simon · L. Vanel · D. Tanguy

Received: date / Accepted: date

Abstract Single crack propagation is studied in a Hydrogen embrittled aluminum alloy. Hydrogen is introduced in the system by electrochemical reactions in an acid aqueous medium. After Hydrogen charging, tensile tests are performed in air, on notched samples, with a micro-tensile machine. An optical microscope is used to follow single crack initiation and propagation at a high magnification. Digital Image Correlation gives the displacement field on the surface with a spatial resolution of about 1 micron. It enables the determination of the position of the crack tip and the local velocity at a sub-grain scale. The equivalent Von Mises strain is calculated and gives a precise measure of the local plastic field which accompanies crack propagation. In addition to the primary plasticity which is emitted from the crack tip or its immediate neighborhood in the form of two intense slip bands, it is systematically found a secondary plastic zone which spreads over several microns ahead of the tip. The characteristics of the plastic zone are measured, together with the velocity and the applied stress intensity factor. In addition, different fracture mechanisms are found on the fracture surface. In particular there are transitions in the fracture mode from intergranular smooth to transgranular parallel to the grain boundary plane. The local fracture mechanisms, in the vicinity of the surface, are linked to the local velocities and plastic deformations. Surprisingly no strong velocity/plasticity correlations are found while the velocities are scattered over a wide range.

Keywords Micro-mechanics · Hydrogen · Embrittlement · Digital Image Correlation

L. Stermann, G. Simon, L. Vanel and D. Tanguy
Institut Lumière Matière, UMR5306 Université Lyon 1 - CNRS, Université de Lyon 69622 Villeurbanne cedex, France
E-mail: dome.tanguy@univ-lyon1.fr

PACS 62.20.Mk

1 Introduction

Environmentally assisted cracking, including hydrogen embrittlement, is a major concern for structural metallic alloys because it causes premature failures at mechanical loads well below those required for purely mechanical fracture. In addition, there is a recent increase of interest for this problem in the context of the reduction of CO_2 gas emission either by the deployment of fuel cell technology or by the development of hydrogen engines for airplanes. The mechanisms at the origin of this phenomenon are intricate and diverse, depending on the material, the environment and the way the mechanical load is applied [1]. Corrosion induced anodic dissolution can be mechanically localized, for example at the surface steps where slip bands emerge [2], or chemically localized, for example at grain boundaries hosting segregations or fine precipitation with one element being preferentially dissolved [3]. This might cause crack initiation. The possibility that localized anodic dissolution is also responsible for fast, crystallographic, transgranular crack propagation, i.e. beyond the initiation stage, in conjunction with localized plasticity or cleavage [4], is still debated (see the references in [5]). Recently, atomic scale observations demonstrated that a strained nanoporous layer, obtained by preferential dissolution of a concentrated binary alloy, can inject a cleavage intergranular crack in the non-dealloyed material, microns ahead of the layer [6]. This mechanism could be active, locally, in alloys with intense intergranular segregation. In addition to this complexity, anodic dissolution often implies the reduction of hydrogen coming from the dissociation of water, in aqueous

media. A fraction of the hydrogen produced is absorbed and diffuses in the material where it causes embrittlement [7]. Here also, the mechanism of fracture is not completely established [8]. Recent high-resolution experimental observations concern: hydrogen-induced dislocation cell refinement in the plastic wake [9], quantified plasticity localization in deformation bands [10], the formation of vacancy-hydrogen clusters revealed by the pinning/depinning dynamics of dislocations in nano pillars [11]. In particular, the fracture of micro-beams in the presence of water vapor inside an environmental SEM, coupled with transmission electron backscatter diffraction, revealed the intensity of plasticity accompanying brittle transgranular fracture with nanometer scale resolution [12]. On the modeling side, atomistic simulations have contributed by evaluating several elementary mechanisms such as: the modification of dislocation emission at crack tips by adsorbed hydrogen [13, 14], the enhancement of equilibrium vacancy concentrations [15,16], the formation of bubbles by aggregation of vacancies produced by dislocations and stabilized by hydrogen [17], the decrease of cohesion related to the segregation of hydrogen [18,19], vacancy-hydrogen clusters [20], voids [21] or dynamic segregation [22] at grain boundaries. Diffusion of vacancies at low [23] and high hydrogen concentration [24] and trapping of hydrogen are also very important issues that have been intensively studied by atomistic simulations [25,26], including pipe diffusion at dislocations [27].

In this context, we develop new experiments with high magnification in situ observations of the fracture processes, that could be useful for developing mesoscale models capable of bridging the gap between atomistic simulations and macroscopic experiments. In this paper, an aluminum alloy is charged with hydrogen and strained with a micro-tensile stage to obtain single cracks. Digital image correlation is used to measure the crack advance and the related plastic deformation at the micron scale.

Aluminum alloys are interesting model systems because they can be prepared in metallurgical states where they are sensitive enough to hydrogen to promote single cracks facilitating in situ monitoring. More specifically, there is a wealth of studies [28] in the AlZnMg and AlMg [29] aluminum alloys. They are immune to dry hydrogen gas because of the high dissociation barrier of the molecule on the oxide [30]. Exposure to a plasma [31,32], which skips this dissociation step, shows hydrogen penetration is effective with the formation of bubbles at the oxide-metal interface [33] or the formation of vacancy-hydrogen clusters further inside the material in nano pillars [11]. In aqueous media, hydrogen comes from electrochemical reactions at the surface involving the dissociation of the water molecule [30] and the subsequent absorption of a fraction of the produced hydrogen. The result is a degradation of the mechanical properties: on macroscopic specimen, a mechanical threshold appears at a stress intensity factor (K) about 5 to 10 MPa$\sqrt{m}$, well below the critical K in the absence of hydrogen [34]. Beyond this threshold, the crack velocity shows a weak dependence on K, until the critical value for catastrophic failure is reached. Water vapor (including lab air), in particular hot water vapor, and chloride containing solutions, are hydrogen producing environments. At room temperature and low relative humidity, crack propagation occurs at velocities of the order of 10^{-10} ms^{-1} that continuously grow with relative humidity until condensation occurs reaching 10^{-8} ms^{-1} (alloy 7075, T651 state) in distilled water (see figure 19.12 and references in [30]). Metallurgical state influences this velocity by one order of magnitude, underaged (resp. overaged) being more sensitive (resp. less sensitive) [34]. Exposure to hot water vapor followed by subsequent tensile test in air results in hydrogen embrittlement [35]. Fracture morphology can be either transgranular or intergranular [35,36]. Hydrogen bubbles have been observed at intergranular precipitate/matrix interface in TEM but are assumed to decrease embrittlement by trapping hydrogen otherwise present along the grain boundaries [35,37]. Coarse intergranular precipitates can indeed have a beneficial effect on intergranular hydrogen embrittlement [36].

The paper is organized as follows: the choice of the material and its preparation are presented, then the digital image correlation (DIC) methodology is illustrated by an example showing the plastic blunting of an intergranular crack and finally the main results are given, including: the measured deformation state at initiation at the notch tip, the different fracture morphologies and the statistics of the local velocities, plastic zone sizes and plastic deformation. Some correlations that were attempted are discussed.

2 Material and methods

The alloy chosen is the aluminum alloy 7108 which chemical composition is given in table 1. It was received as a rolled plate of thickness 8 mm with the microstructure shown on figure 1a. AlZnMg alloys harden by precipitation. The present precipitate phases are the solute clusters, called "Guinier-Preston zones", on the lattice sites of aluminum [38], the semi-coherent metastable η' ($MgZn_2$) and the stable incoherent η phases [39]. Figure 1a shows intragranular precipitates in the shape of plates and rods which are likely different forms of η [40] precipitates in an overaged state, owing to their

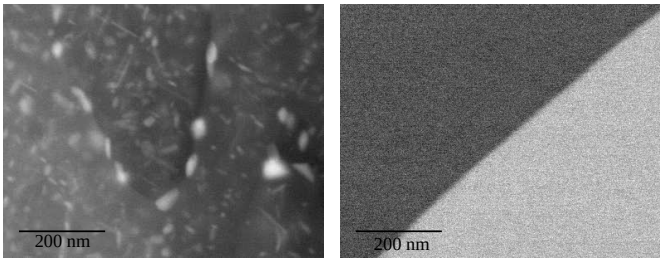

Fig. 1 Microstructure viewed by high resolution scanning electron microscopy (a) as received, (b) after heat treatment and one week natural aging, the precipiates are dissolved.

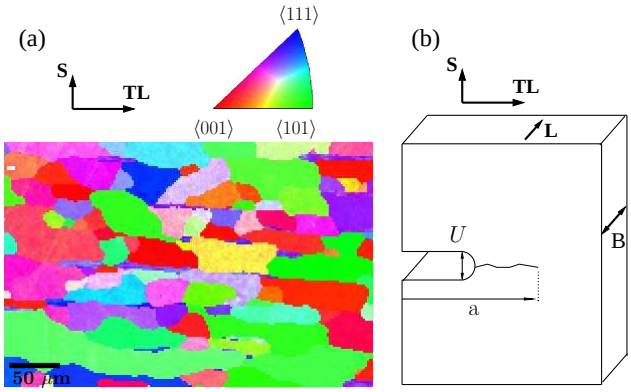

Fig. 2 (a) Electron back scattered diffraction orientation map in the short/transverse long plane, (b) schematic view of the sample.

large size in comparison to the peak aged microstructure [41]. The figure also shows larger, globular, precipitates along the grain boundaries and a precipitate free zone as reported in [42].

The copper content (Tab. 1) is significantly lower than in other commercial alloys where it is around 2.5%. Cu is reported to enter the composition of the intergranular $MgZn_2$ precipitates, increase their density, reduce the localized anodic dissolution rate and accordingly the stress corrosion cracking plateau velocity [43], in a saturated NaCl solution. In other environments, this trend is not confirmed [44]. Moreover different quench rates can also have a drastic effect on the plateau velocity and the link with microstructure is not established [44]. Even with these limitations, we consider that having a reduced Cu content reduces the protective effect Cu segregation could have on GBs with respect to anodic dissolution in wet air conditions, which are the conditions of our tensile tests. In a previous study [45], it was also shown numerically that the presence of generic brittle precipitates (representing H embrittled η precipitates [35,37]) has some minor effect on intergranular cleavage, as modeled by cohesive zones. As a consequence, the choice was made to simplify the microstructure by heat treating the samples, after machining, to eliminate the intergranular precipitates. Samples were held at 400 °C for 1h, followed by a water quench and natural aging. The result is the dissolution of all the precipitates of the as received microstructure and a recrystallisation (Fig. 1b). Some grains are equiaxe, others kept an elongated aspect ratio (Fig. 2a). To take advantage of the latter, the micro tensile samples are machined (by electrical discharging machining) along the short direction (S) (Fig. 2b). The gauge length is 4 mm, the width either 1 mm or 1.5 mm and the total length including the heads 8 mm. A U notch, of initial thickness U_0=70 μm, is cut in the plane normal to S with a front along the long direction (L). As a consequence, the number of grains along the crack front is minimized. The dimension of the samples in this direction (the sample's thickness B) is a parameter. Ideally, the samples could be thinned to have only one grain in the thickness so that the slip orientation observed on the side surface are representative of the crystallography all along the crack front. The real grain structure is far from this idealness. The grain size is heterogeneous (Fig. 2a) as observed on a EBSD map in the S-TL plane and on the fracture surfaces on the L-TL plane, with some equiaxed grains of diameter of the order of 20 μm and others keeping an elongated aspect with dimensions up to 200 μm in the L direction. The average grain thickness (the dimension in the S direction) is 17 μm (+/- 9 μm). Finally, there are indeed portions of the samples with long, flat intergranular facets oriented perpendicular to the S direction, but usually, the thickness contains many grains, some of them equiaxe. The thickness B is varied between 0.2 mm and 1 mm.

The samples are polished mechanically with diamond pastes containing particles of diameter down to 1 μm. Hydrogen is introduced in the material by an electrochemical process. The samples are immersed in a sulfuric acid solution (pH 2.0) in a 3-electrodes cell. A cathodic potential E_c is imposed during a charging time t_c. All the electrochemical potentials are measured with respect to a reference which is a saturated calomel electrode (SCE). The mechanical tests are done in lab air after the sample is taken out of the acid and dried. The relative humidity is in between 40 and 60% and the temperature about 22 °C in the room.

H induced cracking is strain rate dependent [46,47]. Therefore, it is important to define how the sample is stressed and what is the criterion to decide if a crack propagates. The force on the sample is raised in steps at the minimum jaws' velocity allowed by the machine (0.005 mm/min i.e. a strain rate of $\dot{\epsilon}_0 \approx 2 \times 10^{-5} s^{-1}$). When the target force F is reached, the displacement of the jaws is fixed. A mechanical relaxation occurs which

Table 1 Measured composition of the AA7018 alloy (weight%).

Si	Fe	Cu	Mn	Mg	Cr	Ni	Zn	Pb	Ti	Zr	Al
0.0308	0.0804	0.0116	0.0099	1.23	0.0016	0.0104	4.995	0.0004	0.0352	0.1417	base

lasts about 5 min. Beyond this time, the onset of the force drop due to crack propagation requires a certain initiation time. It was observed that if no drop is detected after 20 min, propagation never starts within the next 2 hours (a few tests were made with a waiting period of 12 hours, which compares with the total duration of the experiment) and therefore, a waiting time of about 20 min in between two force raises is appropriate to detect crack initiation and propagation. The crack length a (Fig. 2b) is measured on the side of the sample by DIC. The mechanical load is characterized by the stress intensity factor K defined from F and a as (see [48] for a "Singled Edge Notch Test" specimen):

$$K = f(a/W)\sigma_\infty\sqrt{\pi a} \quad (1)$$
$$f(a/W) = 1.12 - 0.23\frac{a}{W} + 10.56(\frac{a}{W})^2 - 21.74(\frac{a}{W})^3 + 30.42(\frac{a}{W})^4$$

where W is the width of the sample and σ_∞ the remote stress. The applicability of the formula in our case was checked by finite element calculations.

Finally, the parameters of the experiment are: those of the hydrogen charging (E_c and t_c) and the thickness B of the sample. The load is controlled by the application of the force. The micro tensile stage is placed under an optical microscope and images are periodically taken enabling the determination of the crack length on the side of the sample by DIC. K is therefore known all along the test and is reported at initiation. The deformation of the notch $\epsilon_{notch} = \frac{U}{U_0}$ at initiation is also measured. U is the opening of the notch at the edge of the circular tip, as defined on figure 2b. Before the results are given, the DIC method is detailed.

3 Digital image correlation

The exposure of the polished surface to the H_2SO_4 solution generates an attack of the surface which reveals the grains and the grain boundaries. When observed in optical microscopy, the rough surface state creates a speckle (Fig. 3) that is used to measure surface displacements by digital image correlation [49]. The method used is the "Lucas Kanade Feature Tracker" as implemented in the OpenCV library following the algorithm by Bouguet [50] and called with the Python interface "pydic" [51]. The correlation between two images gives a displacement field that is called "incremental" to differentiate it from the displacement field which is the sum over all the incremental fields of the sequence of images, starting from an initial configuration with no plastic strain, crack and stress.

At the microscope's maximum magnification of $\times 2000$, the pixel size is 110 nm. The grid size is 10×10 px^2, i.e. the maximum spatial resolution is about one micron. The noise level is estimated by taking consecutive pictures without strain and correlating them. With a correlation window of 40×40 px^2, the noise level is about 0.1 px, meaning a background noise of amplitude 1% in the measure of the deformation. Therefore, only large plastic deformations are measured which is already enough to meet our goals: determination of the crack tip position and measurement of the plastic deformation in the vicinity of the crack tip. An example is shown on figure 3. It represents the blunting of an intergranular crack followed by a fracture event. Two slip bands are present, in the grains above and below the intergranular crack plane, originating from two distinct sources slightly shifted along the crack propagation direction. They are originally both active during the blunting stage while, during fracture, only the upper one, associated to the crack tip, is active. At a later stage, the crack continues to propagate intergranularly in a semi-brittle manner but with a reduced plasticity production. The displacement field associated to the blunting in the near tip region could not be obtained because the speckle changes too much at this location. This two stages process is visible in the asymmetry of the "incremental" crack opening profile (the opening component of the displacement field u_y, y being the orientation of the tensile axis) (Fig. 4a). Two plastic lobes are also visible in the "incremental" strain map of figure 4b. On the upper left corner, the focus is lost and this part of the image could not be used for DIC. The measured "strain" is the in plane equivalent strain ϵ_{eq}:

$$\epsilon_{eq} = \frac{2}{3}\sqrt{(\epsilon_{xx} - \epsilon_{yy})^2 + 3\epsilon_{xy}^2} \quad (2)$$

For comparison, an example of intergranular crack propagation is also given (Fig. 4c and d). Note the reduced plastic deformation (in intensity and spreading) and the difference in angle between the crack plane and the plastic lobes which is the signature of the crystallography. The opening angle is defined as $\alpha = 2\tan^{-1}\frac{\Delta u_{yc}/2}{\Delta a}$

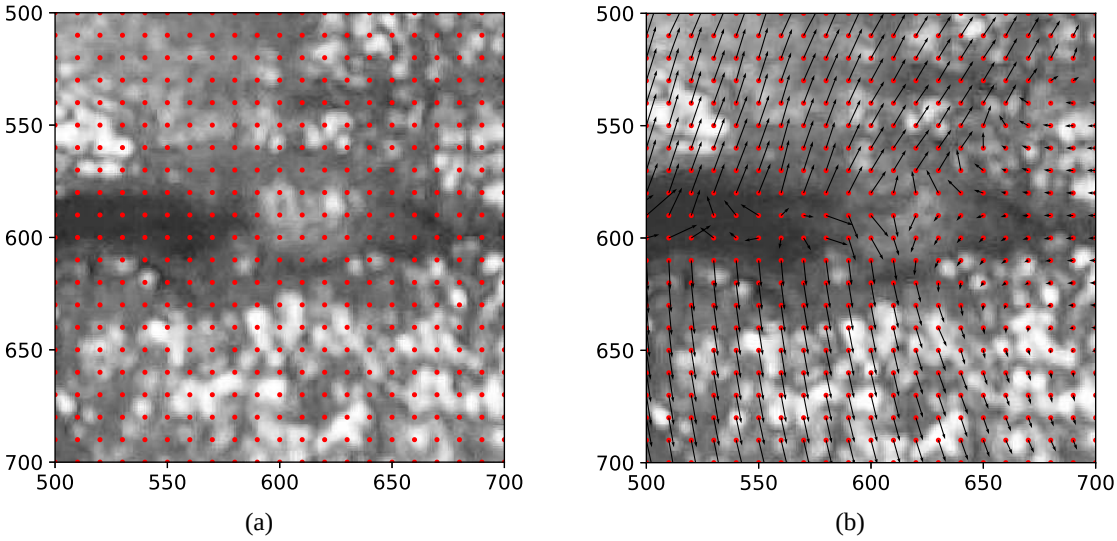

Fig. 3 A zoom on the crack tip of sample D viewed by optical microscopy (10 px = 1.1 μm). (a) The DIC grid superimposed to image A (step 10 px = 1.1 μm). (b) Image B, after a crack advance, with the displacement field (arrows) obtained by correlating image A with image B (correlation window 40×40 px^2).

where Δu_{yc} is the opening of the crack measured on the "incremental" crack opening profile and Δa is the increment of crack length. It was found that the distance in between the end of the flat part of the "incremental" crack opening profile and the crack tip position (f on Fig. 4c) is close to the value of Δa measured by taking the difference in crack tip position between two images, within the limitation of the precision, about 1 μm. This means that the plasticity which emerges at the crack lips is essentially produced at or in the immediate vicinity of the moving crack tip and not from fixed remote sources.

The position of the crack tip can now be defined. A particle sitting exactly on the crack path, ahead of the crack tip, would have zero displacement, by symmetry, while particles slightly off plane would be displaced further away either elastically or by the processes active ahead of the crack tip in the non linear "process zone". Behind the crack tip, such particles do not exist, they are all either above or below the crack plane. Therefore, the displacement field changes sign, with a discontinuity behind the crack tip while this occurs continuously, going through zero, ahead of the crack tip. Depending on the position of the grid with respect to the crack plane, this effect might be directly visible on the grid points. Otherwise, if the crack runs in between two rows of grid points, the displacements have to be extrapolated, and this introduces some subjectivity. In addition, the fact that intense slip bands intercept the crack plane at or behind the crack tip [52] is also used as a guide to decide were the crack tip is. And finally, it is also considered that the opening deformation at the crack tip, estimated by the difference in the displacement of the grid point one row above and one row below the crack path, divided by one grid spacing, cannot be too large (smaller than 100%). In the two examples of figure 4 a and c, the crack tip positions are respectively 650 and 760 px. The incremental deformation at the tip ϵ_{yy}^{tip} is defined as:

$$\epsilon_{yy}^{tip} = \frac{u(y^+) - u(y^-)}{y^+ - y^-} \tag{3}$$

where y^+ and y^- are the positions above and below the crack plane, at the crack tip. ϵ_{yy}^{tip} is incremental, however, the consecutive images are seldom taken close enough in time to resolve the dynamics of the formation of the plastic zone in the first microns ahead of the crack tip (Δa is always larger than the plastic process zone, as will be shown below), except when the velocity is very low (4 μm/h and below), for example in figure 4 a (blunting). Therefore, the measurements represent the complete deformation of the tip. If the grid runs in between two rows of grid points, $y^+ - y^- = 10$ px, otherwise, if a row of points have small displacements, it means that the crack runs close to this row and the deformation is estimated from the rows above and below this row ($y^+ - y^- = 20$ px). When the correlation window is bigger that the grid step, the displacements are smoothed. This introduces a bias in the deformation. Window sizes of 20, 30 and 40 px were tested. Qualitatively, the displacement field remains the same, except in the vicinity of the tip. Indeed, ϵ_{yy}^{tip} takes the values, respectively, of 2.3%, 8.4% and 26%, while if the measure is made by taking the values one grid step further

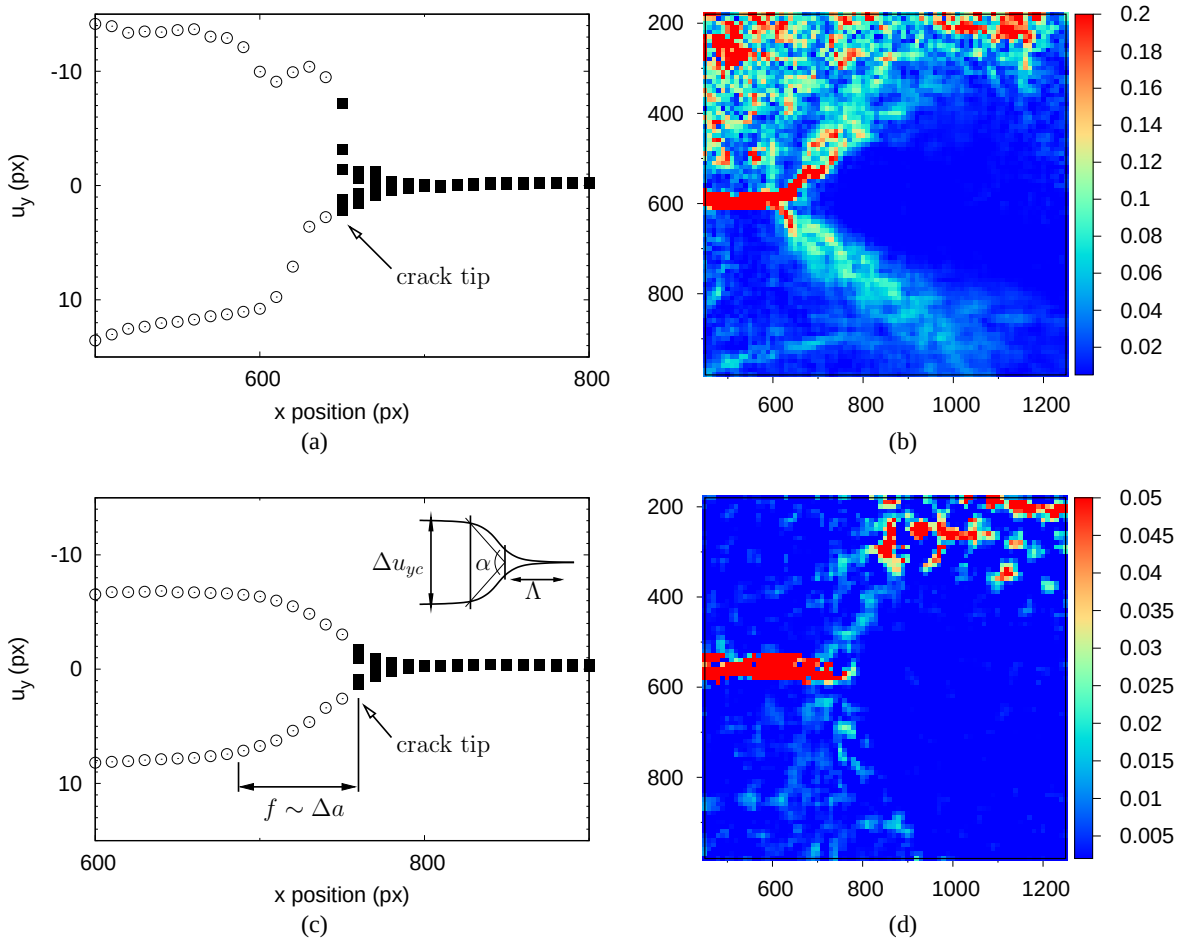

Fig. 4 Incremental crack opening profiles (a and c) and equivalent strain maps (b and d) obtained by DIC of two pairs of images. (a) and (b) illustrate crack blunting followed by a transgranular crack advance (the two consecutive crack configurations are the same as those used for figure 3). (c and d) are representative of brittle intergranular cracking. The symbols in black on the profiles represent the displacement in y, ahead of the crack tip. For one position in x, the different symbols represent different planes (y=-20, -10, 0, +10 and +20 px from the crack plane). The open symbols represent the opening at the back of the crack tip. The crack tip is at x=650 px, y=585 px, in between two rows (resp. x=760 px, y=565 px) in (a) and (b) (resp. in (c) and (d)). The insert in (c) defines the crack opening angle α, the length Λ of the "plastically deformed zone" along the crack path, ahead of the tip and the increment of crack opening Δu_{yc}. f is the distance between the end of the flat region of the profile and the crack tip (see text).

away from the crack plane, i.e. $y^+ - y^- = 30$ px, ϵ_{yy}^{tip} is respectively: 14%, 15% and 18%. On the one hand, this window size effect comes from the proximity of the primary slip bands with the crack tip and the smoothing inherent to the DIC method which forces the continuity of the displacement field. On the other hand, if not broken the matter is continuous and the displacement should be a continuous interpolation between the displacement of the two primary slip bands. The method used is qualitatively correct, but is not accurate enough and spatially resolved enough to precisely measure ϵ_{yy}^{tip}. A more performant method, based on particle tracking, is discussed at the end of the paper. Together with ϵ_{yy}^{tip}, the length Λ of the deformed region ahead of the crack tip is also measured (Fig. 4c). It starts at the crack tip and ends when $u(y^+) - u(y^-)$ falls within the noise, i.e. below 0.1 px.

4 Internal hydrogen induced cracking results

A reference test, without hydrogen charging, was done in laboratory air. The relative humidity was of the order of 65%. The force was raised above the yield point (at 5% strain, $\sigma_{max} = 175$ MPa, $\epsilon_{notch} \approx 65\%$, Tab. 2) after which the displacement of the heads of the sample was fixed. The force dropped at a constant rate. After 18 days, a 3 μm long crack appeared on the surface at the tip of the notch, together with a sudden increase in the force drop rate. This is considered as the initiation time. The corresponding stress intensity factor is

Table 2 Characteristics of the tests done: sample name, cathodic electrochemical potential E_c, hydrogen charging time t_c, maximum stress σ_{max} (force divided by the initial section, not taking into account the notch), notch deformation ϵ_{notch}, applied stress intensity factor K (at initiation and at the end of the single crack propagation), average crack velocity $\overline{v}$, maximum local velocity v_{max}, sample thickness B. The velocities marked with a star were not obtained by DIC.

Sample	E_c mV/SCE	t_c h	σ_{max} MPa	ϵ_{notch} %	K MPa$\sqrt{m}$	$\overline{v}$ μm/h	v_{max} μm/h	B mm
air	-	-	175	65	11	3	-	1.0
A	-1300	48	190	64	22	7*	7*	0.4
B	-1400	72	158	39	10 - 11	15	96	0.5
C	-1400	24	164	53	13 - 15	25*	25*	0.4
D	-1500	72	126	34	23 - 26	33	101	0.6
E	-1500	24	121	39	18 - 22	22	79	0.7
F	-1600	48	145	11	5 - 9	120*	130*	0.2
G	-1600	24	156	24	5 - 13	262	435	0.2
H	-1600	48	145	19	7 - 12	176	1800	0.6
I	-1600	28	162	25	8 - 14	254	528	0.6
J	-1600	24	155	18	8 - 12	65	144	0.4
K	-1600	65	155	22	7 - 12	338	480	1.0

K=11 MPa$\sqrt{m}$. During the steady propagation stage, the crack was stopped and restarted by placing the experiment under dry nitrogen gas followed by a return in wet air after 2 hours (restarting the crack took 12 h) which confirmed the role of the wet environment in agreement with literature [30]. The crack velocity, estimated by the evolution of the trace on the surface, was of the order of 3 μm/h ($10^{-9}m/s$ also in good agreement with [30], figure 19.12). The fracture surface (Fig. 5a) is the result of a single planar transgranular crack which propagated through the entire section of the sample except for a reduced final shear lip.

Eleven other tests were also conducted in lab air but after hydrogen charging in different conditions presented in table 2. A macroscopic side view of the sample (sample G in table 2) after the complete propagation of a crack is shown on figure 6. During hydrogen charging, the electrolyte attacked the surface and revealed some of the grains. Multiple short cracks are visible from the notch tip. The main crack emerged from one of them and propagated as a single crack perpendicular to the tensile axis for about 300 μm. The data are always collected from this phase of the tests. In the final stage, the crack deviates, plastic deformation is intense and multiple cracks form.

The macroscopic results of table 2 show that the major parameter for embrittlement (low K at initiation and high average propagation velocity) is the applied cathodic potential E_c at the expense of the charging time, within the range studied, i.e. all samples were exposed to the electrolyte for more than 24 h. The trend is that the deformation required for initiation decreases with applied potential. In the absence of hydrogen charging, it is as high as 65% and decreases down to an average of 20% at -1600 mV/ECS. The average crack velocity is also clearly dependent on E_c with a slow velocity of 7 μm/h at -1300 mV/ECS, an average of 24 μm/h for the four samples at intermediate potentials -1400 and -1500 mV/ECS and a significantly higher velocity at -1600 mV/ECS of 200 μm/h. In the appendix, figure 10 presents a more detailed view of the deformation before the formation of the first cracks at the bottom of the notch. DIC shows the extent of the deformation and its repartition ahead of the notch. Initiation always occurs at the point of maximum deformation, which can be at one corner of the notch or at its center, depending on the geometry and the way the notch changes shape when the mechanical load is raised. It is interesting to see that the scale of the area over which the concentration of deformation, responsible for initiation, occurs is at least 20 μm (the area deformed beyond 10% is 2×2 px^2 in figure 10f), which is of the order of the grain size. A physical criterion for initiation should involve the local deformation within this zone and the stress concentrations that it creates [53–56] but this would require observations at a spatial resolution higher than the one reached in this study. The deformation maps (Fig. 10) also show that, in the most brittle cases, the prestraining due to the notch is very limited passed the first 100 μm ahead of the notch tip. For example, it is below 0.01 on figure 10f. Therefore, the single cracks propagate in samples essentially free from pre-deformation (even if this might enhance propagation).

4.1 Local crack velocities

Once the main crack has detached from the assembly of short cracks formed at the notch tip, local propagation velocities can be measured. Out of the 11 samples

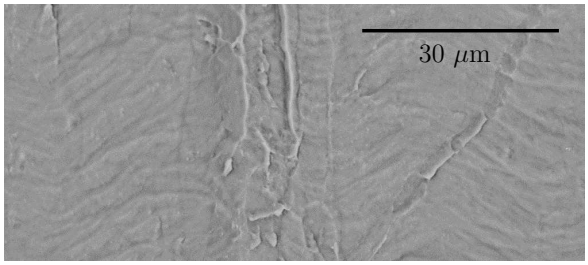

(a)

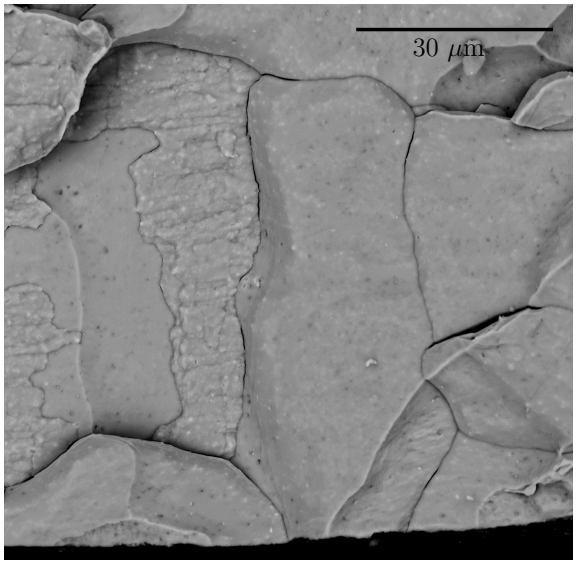

(b)

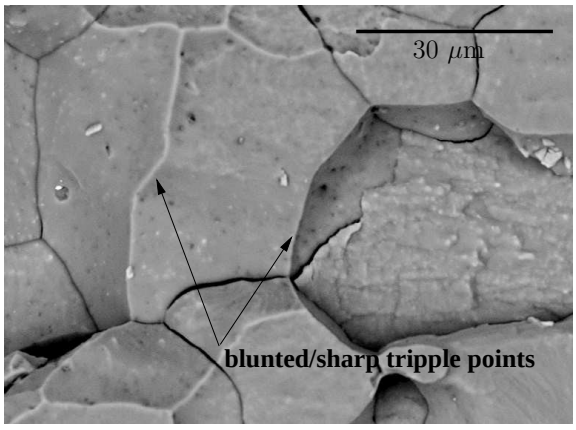

(c)

Fig. 5 (a) Fracture surface of the reference test in humid lab air. (b) Typical fracture surface in air after electrochemical hydrogen charging. It is composed of a mixture of transgranular and intergranular fracture (sample J, Tab. 2). (c) Blunted/sharp broken tripple points (sample G, Tab. 2).

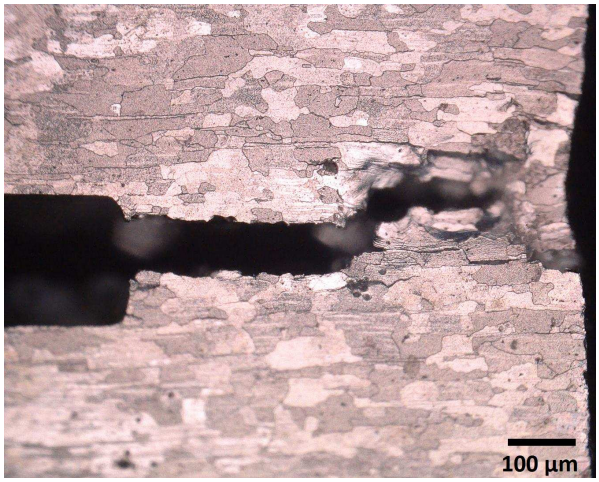

Fig. 6 Macroscopic optical view of the side surface of sample G ($E_c = -1600$ mV/ECS, $t_c = 24$ h, $K = 5$ MPa$\sqrt{m}$, Tab. 2) close to final fracture.

fractured (Tab. 2), only 90 crack tip positions could be determined. The limitations to such measurements are: the quality of the pattern which is not homogeneous among the samples, and the out of plane plastic deformation, which can be too large close to the crack tip to allow the measurement of the incremental crack opening profile. 80 local velocities were determined, 60 were from DIC, the others only from the gray level of the images. Among the 60, only 50 were considered representative of "propagation". For example, the very large velocities, some as high as 1800 μm/h, result from the sudden emergence of cracks running just below the surface and their apparent merging with an arrested surface crack. Such cases were discarded and the maximum local velocity v_{max} is about 500 μm/h.

As already mentioned, there is a marked difference in velocity depending on the electrochemical potential applied during the hydrogen charging. The propagation velocity is markedly enhanced when the potential is decreased to -1600 mV/ECS. Even if the hydrogen content was not estimated, it is reasonable to consider that a lower potential involves a higher hydrogen content. Therefore, the samples are split in two groups: B, D and E constitute the "low hydrogen content" group (LH group) (A, C and F did not allow local measurements) and G, H, I, J and K constitute the "high hydrogen content" group (HH group). The corresponding velocity distributions are shown on figure 7a for the LH group and figure 7b for the HH group with an average of 24 μm/h and a maximum of 111 μm/h, and an average of 200 μm/h and a maximum of 480 μm/h, for LH and HH respectively. In order to obtain the best possible images, the focus is adjusted by hand before every image which limits the time resolution to one minute

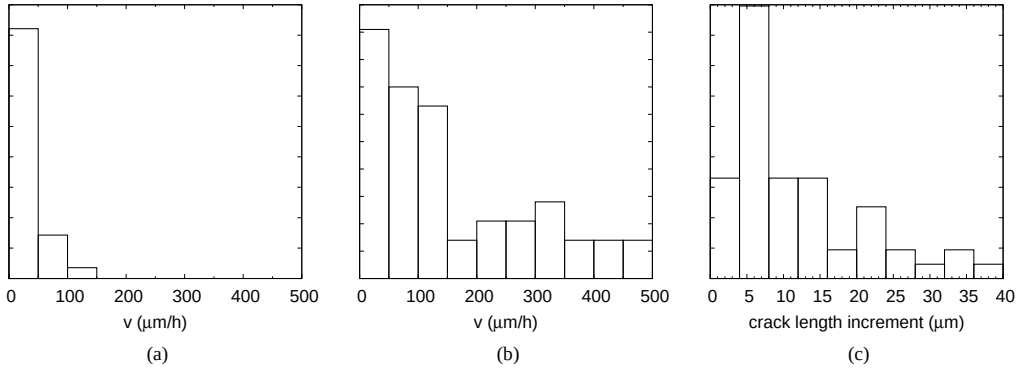

Fig. 7 Local crack propagation velocity distribution v for samples B, D and E (a) which are charged with hydrogen at moderate potential, and H,I,J,K which were charged at -1600 mV/ECS (b). (c) The distribution of the crack increments Δa obtained from the crack tip positions measured on the incremental crack opening profiles from DIC.

maximum. Even then, the quality of the image does not alway allows to correlate properly two consecutive images and the time (and therefore spatial) resolution in crack velocity is usually larger. It is illustrated by the distribution of crack length increments Δa in figure 7c that can be compared to the distribution of grain size along the crack propagation direction, the "transverse long direction" (figure 11 in the appendix). The distribution of crack increments goes from 1 to 36 μm, but is peaked around 6 μm (average 11 μm). The grain size distribution is bimodal (Fig. 11b) with small grains of size about 15 μm and larger grains of size about 45 μm (up to 100 μm). Apart from the small grains, the amplitude of the crack length increments Δa is such that several measurements can be obtained along a GB facet, in case of intergranular cracking, or inside a grain in case of transgranular cracking. The local velocities were also systematically correlated with the fracture mechanism, determined by post-mortem observation of the fracture surface. No correlation appeared between sudden changes in v and changes in fracture mechanisms (for example a transition between intergranular and transgranular cracking). It should be specified that LH samples showed only intergranular crack propagation with different (not quantified) roughness, while HH experienced intergranular cracking with a low roughness (not quantified) and transgranular cracking (quasi-cleavage). This difference in roughness, between LH and HH samples, could be a sign of less embrittlement and more plasticity. The distribution of Δa also gives an estimate of the spreading of the error made on the velocity. Knowing that the accuracy on the crack tip position is at best 1 DIC grid step (1 μm at maximum magnification), the relative error is $\Delta v/v \approx 1/\Delta a$ which is in between 100% and 2.5% depending on the value of Δa (16% for Δa =6 μm). It can be mentioned that whatever the H content and the fracture mechanism, all cracks arrest or nearly arrest at obstacles (they are restarted by applying a small force increment). This is frequent when a triple point at grain boundaries is met. An intergranular crack was observed to blunt when approaching a triple point, arrest, and re-initiate slightly ahead on the next GB facet (off plane). Finally, the region in between the two fractured grain boundaries was fractured by plastic glide. This plastic process modifies the appearance of the triple points on the fracture surface (bottom of Fig. 5b and c). They appear blunted while they are usually sharp when the grains are equiaxed and the fracture can change GB facet by pure decohesion.

4.2 Plastic deformation

The displacement field obtained by DIC also enables to measure the plastic deformation tens of microns around the crack tip. The strain field, although noisy and limited to deformations higher than 1%, highlights the plastic lobes which accompany crack advance (Fig. 4b and d). This is called "primary plasticity". It originates from the shear stress concentration at the crack tip. In the two examples on figure 4b and d, the plastic lobes are not straight and spread over several grains, therefore they are not composed of a single glide system but more likely by several, furthermore in several grains. However, there is a clear difference in the angle between the two lobes between figure 4b and d, which might be of crystallographic origin. As a consequence, it is likely that several sources are activated and not only those at the crack tip or at its immediate vicinity. The incremental crack opening profiles often show that most of the plasticity that emerges at the crack surfaces originates from "moving sources" related to the crack tip. Therefore the crack opening angle α is a measure of only part of the plasticity created during crack ad-

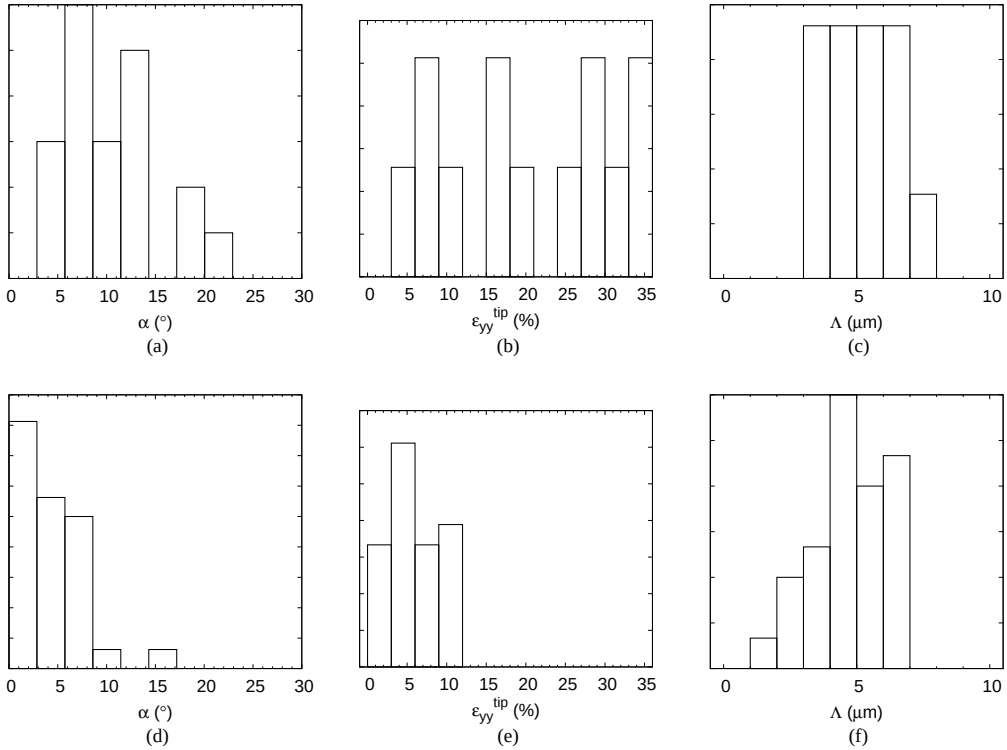

Fig. 8 Graphs a, b and c correspond to the group with a low hydrogen content (LH) while d, e, f correspond to the one with a high hydrogen content (HH). (a, d) Crack opening angle α, (b, e) deformation in the first micron ahead of the tip ϵ_{yy}^{tip} and (c, f) length of the process zone (Λ) ahead of the tip.

vance. Nevertheless, it is taken as a first measure of plasticity because it is a robust quantity, easy to measure on the profiles. The distributions of α for the LH and HH groups are given on figure 8a and d respectively. Plasticity is clearly reduced in the HH case in comparison to the LH case.

In addition to the crack opening angle, the distribution of ϵ_{yy}^{tip} and Λ, which characterize the deformation ahead of the crack tip are given on figure 8b, e and c, f respectively, for the HH and LH groups. When excluding the highest values of ϵ_{yy}^{tip} which correspond to crack arrests on triple points, the average values are respectively 5.8% and 17% for the HH and LH groups. The difference in Λ is much less pronounced with averages of 4.4 μm and 4.7 μm for the HH and LH groups respectively. There have been post mortem characterization of this deformation in TEM [9] and in high resolution EBSD [12]. It was suggested that [9] hydrogen accelerates the evolution of the dislocation structure and stabilizes it in configurations where the dislocation density is higher than at comparable deformation without hydrogen, and that this microstructure favors the development of cracks. In our system the samples also contain hydrogen, initially distributed in the bulk, but they are not pre-strained prior to the expansion of the cracks. The "secondary plastic zone", which is situated just ahead of the crack tip and moves along with it, can reach high tensile deformations, in particular in the case were the H content is supposed to be low (LH), but where the intergranular fracture is conserved. This observation seems compatible with the idea promoted in [9] that some plastic deformation acts together with hydrogen to embrittle the grain boundaries. At the same time "primary plasticity" shields the external load and acts against crack propagation.

5 Discussion

The cracks observed in this work stem from several intricate phenomena and related parameters. The initial distribution of hydrogen after cathodic charging c_0 is supposed to be homogeneous. On the contrary, the strain field produced by the notch and the step by step rise of the force is highly inhomogeneous (Fig. 10). The time taken by initiation is long enough (typically 2 hours) to allow hydrogen redistribution, even at the scale of the whole sample by a combination of desorption, trapping in the strain field, with possibly additional very localized absorption from wet air in relation with localized strain at the notch tip. Later on, dur-

ing the single crack propagation stage, the primary and secondary plasticity (Fig. 4 and 8) might have several roles: to elastically shield the crack tip from the applied mechanical load K, to redistribute hydrogen in more elastically deformed regions or trap it in the plastic wake, or maybe even, in the case of secondary plasticity, to directly participate in the cracking process [9].

A first point to discuss is the delicate problem of effective diffusion in aluminum alloys. At the scale of the whole sample, the distribution of H after cathodic charging, and also during the fracture test, was evaluated by macroscopic diffusion calculations using effective diffusion coefficients and Fick's law (assuming ideal desorption under stress with zero concentration at the surfaces and ignoring the trapping related to plasticity [57]). The hydrogen effective diffusion coefficient D_{eff} describes the diffusion of H as an interstitial atom in the lattice taking into account the trapping/detrapping from crystalline defects, precipitates... Therefore, it depends on the alloy and on its metallurgical state. Young and Scully [58] have measured diffusion coefficients by isothermal desorption at moderate temperature and extrapolated the data to 25 °C. They obtained $D_{eff} = 10^{-11} m^2 s^{-1}$ for the alloy 7050 in the underaged state, a material which is similar to ours. However, it was recently demonstrated that the apparent diffusion coefficient is quite strongly influenced by the initial state of the system. For pure Al, $D_{eff} = 10^{-14} m^2 s^{-1}$ if the sample is free of hydrogen initially and increases up to $10^{-12} m^2 s^{-1}$ when the sample already contains H [59,60]. This is interpreted as a concentration dependence [61], with a faster apparent diffusion when the traps are filled (i.e. when the average concentration is high). Note that in a previous study [36], in the same material as ours, H embrittlement was found to be coherent with $D_{eff} = 2 \times 10^{-12} m^2 s^{-1}$ and not with the slower effective diffusion coefficients. We consider that the diffusion coefficient from Ai et al. [59] is the most reliable because it was determined at room temperature and not extrapolated from high temperatures. Similar values have also been found independently by Hebert [59]. Therefore, $D_{eff} = 10^{-12} m^2 s^{-1}$ is taken as the diffusion coefficient after the H uptake from the cathodic charging (assuming the traps are filled). This is a strong statement. If the effective diffusion coefficient is $10^{-14} m^2 s^{-1}$, then the uptake by diffusion would be limited to the first 100 μm below the surface. It would not be coherent with the hydrogen affected depth which extends in our experiments over the whole sample thickness, even when the thickness is 1 mm long. An argument, sometimes found in the literature, is that "dislocation transport" is the reason why H affects fracture deep in the material. In our case, the primary plasticity is oriented in such a way that it would transport hydrogen towards the mid thickness of the sample and therefore these arguments are not relevant to our case. Finite elements calculations, with this effective diffusion coefficient, show that a sample 500 μm thick retains 20% of its original hydrogen content after 10 hours, which is the maximum duration of the test. Crack propagation is also not diffusion rate limited at the maximum velocity of 500 μm/h [62] with this diffusion coefficient.

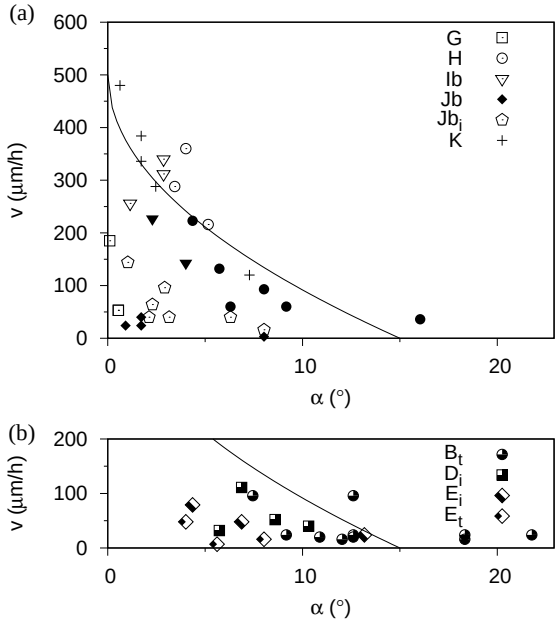

Fig. 9 Local velocity as a function of the crack opening angle: (a) high hydrogen content, (b) low hydrogen content. The lines are a guide to the eye corresponding to $v = v_0(K, C_H)(1 - \sqrt{\frac{\alpha}{\alpha_0}})$ with $v_0 = 500$ μm/h and $\alpha_0 = 15°$.

Embracing all the different aspects is not the goal of this discussion, but we already have a series of parameters: K, E_c, and a number of quantities measured, v, α, Λ... from which we would like to attempt extracting meaningful correlations. Atomistic simulations of intergranular fracture by nano-ductility [21] have shown how a nano scale process zone develops in the case of a strong embrittlement by nano voids. It was shown that the nanoscale non linear process zone expands when the applied load increases. During this stage a dislocation can be emitted if the local cohesive stress is large enough so that the applied elastic stress creates a bending of the crack opening profile at the origin of an incipient dislocation core. Therefore, the ease of producing dislocations at the crack tip (or in the nanoscale fracture process zone) is intimately related to the competition between an increasing elastic stress applied to

the process zone and the relaxation of this stress by the fracture mechanism itself.

The opening angle α is expected to be proportional to the ratio between the dislocation emission rate ν and the crack velocity, both result of the competition mentioned above. An extra complexity comes from the emission of the dislocations which creates the primary plastic zone which in turn shields the applied stress and therefore has a retroaction on the dynamics of the process zone formation, i.e. on ν and v. It is expected that, if the system is more embrittled, the dislocation emission is reduced. As a consequence, we take α as a parameter which expresses the degree of brittleness of the fracture process zone and plot v (the other local data representative of fracture that we could measure) as a function of α (Fig. 9). HH and LH are represented on different graphs, but the same curve is used as a guide to the eye to compare the two data sets. The trend is as expected: if α is large, v is small, eventually zero (complete blunting, like in the case of a mechanical overload). In the LH case, no crack propagation was observed if α is below 4°, while at higher H content, large velocities are observed with a low opening angle. This suggests that either the shielding by primary plastic lobes is not completely efficient so that raising K gives a higher local stress, necessary for GB fracture at low hydrogen concentration, or, the secondary plasticity is part of the embrittlement process, or both. It can be noticed that transgranular fracture (in full symbols on figure 9a) is slower that intergranular fracture, if the maximum velocity at constant α is considered. No transgranular cracks ran faster than 250 μm/h.

One puzzling aspect of the data is that whatever the α value, there are cracks with almost zero velocity. This is conceavable if crack advance requires a threshold local stress and if the stress felt at the crack tip falls below this threshold because of the turtuousity of the crack (many grains exist in the thickness, even in the thinnest cases, and secondary cracks, parallel to the main crack, are observed on the fracture surface).

6 Conclusion

Embrittlement of an AlZnMg alloy by internal hydrogen was studied experimentally by means of micro tensile tests. Single cracking was favoured by notching the samples, and the mechanical load was imposed by fixing the displacement of the grips. Crack propagation was followed on the surface by optical microscopy. The displacement field was measured by digital image correlation with a resolution of 1 μm. The crack positions, and therefore the local propagation velocities, were determined, but also the plasticity produced by the crack advance. A correlation was attempted between the velocity and the opening angle, measured from the crack opening profile, representing the rate of dislocation emission from the fracture process zone. The expected tendency where the crack velocity decreases when more dislocations is injected in the system is retrieved but, whatever the crack opening angle, low propagation velocities are always observed. Indeed, the velocities are scattered between 4 and 500 μm/h in the most brittle cases. Furthermore, fracture occurs by a rich variety of mechanisms mixing transgranular and intergranular cracking. No strong correlation was found between the local crack velocity and the nature of the crack, even if the largest velocities (beyond 250 μm/h) always correspond to smooth intergranular cracks.

The experiment suffers from a number of limitations, in particular: the number of exploitable images per tensile test is low, because the quality of the surface pattern and the focus of the image are not always ideal for DIC; the resolution (1 μm) is sufficient to image primary plasticity but is too limited to have a clear picture of the secondary plasticity. Future work will be dedicated to the development of cracking experiments within an SEM to better characterize secondary plasticity, in interaction with simulations.

Acknowledgements This work used the equipment from the Optolyse platform (ILMTech). We gratefully acknowledge V. Motto-Ros from Institut Lumière Matière, P. Pittet from Institut des Nanotechnologies de Lyon and O. Dezellus and B. Gardiola from Laboratoire des Multimatériaux et Interfaces for their help in preparing the experiments.

7 Appendix

References

1. Pydic is a free suite of Python tools for local digital image correlation analysis, by Damien André. https://gitlab.com/damien.andre/pydic
2. Pyramidal Implementation of the Lucas Kanade Feature Tracker description of the algorithm. J.-Y. Bouguet, Intel Corporation, 2001. http://robots.stanford.edu
3. Ai, J., Scully, J.R.: Hydrogen diffusivity during corrosion of high-purity aluminum. corrosion **69**, 752 (2013)
4. Ai, J.H., Lim, M.L.C., Scully, J.R.: Effective hydrogen diffusion in aluminum alloy 5083-H131 as a function of orientation and degree of sensitization. Corrosion **69**, 1225–1239 (2013)
5. Badwe, N., Chen, X., Schreiber, D.K., Olszta, M.J., Overman, N.R., Karasz, E.K., Tse, A.Y., Bruemmer, S.M., Sieradzki, K.: Decoupling the role of stress and corrosion in the intergranular cracking of noble-metal alloys. Nature Materials **17**, 887–893 (2018)
6. Ben Ali, N.: Caractérisation et modélisation micromécanique de la propagation de fissures fragiles par effet de l'hydroène dans les alliages AA7XXX. Ph.D.

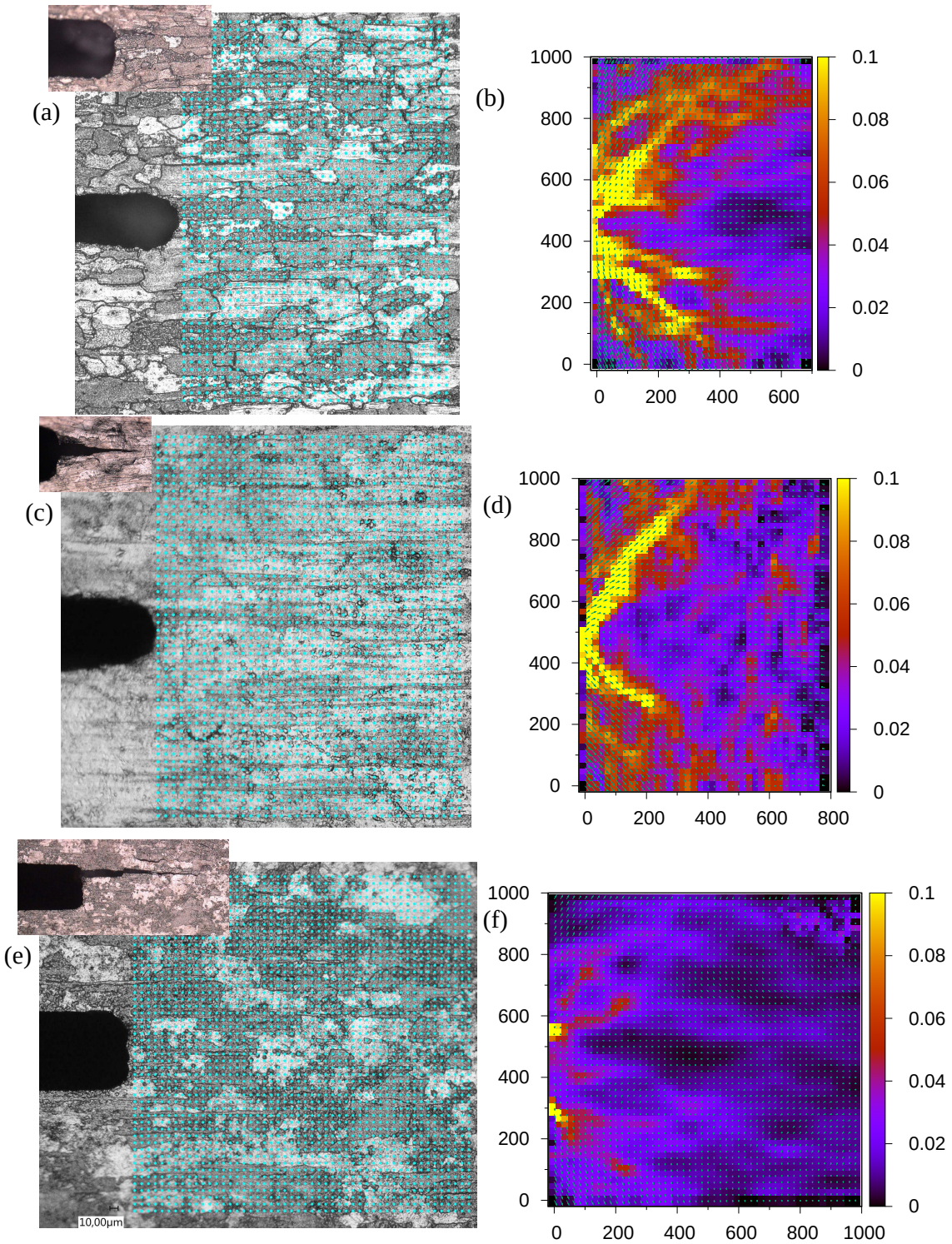

Fig. 10 Illustration of the local strain necessary for crack initiation from a notch. Images (a,b), (c,d) and (e,f) correspond respectively to samples D, E and J (Tab. 2), i.e. to H charging conditions (E_c=-1500 mv/SCE, t_c=72 h), (E_c=-1500 mv/SCE, t_c=24 h), (E_c=-1600 mv/SCE, t_c=24 h), respectively. Pictures on the left are optical images of the surface used for DIC. The grid is superimposed. On the right are the corresponding Von Mises deformation maps calculated from the displacement field. The axis units are in pixels (px) with 20 px = 12 μm, which is also the grid step length. For example, (b) is 700 px x 1000 px = 414 μm x 593 μm. The inserts show the cracks emerging from the notch tip.

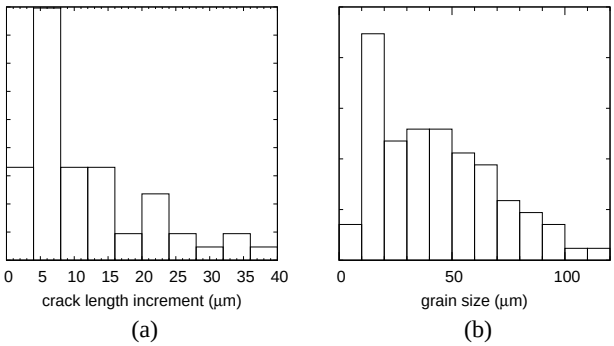

Fig. 11 (a) Crack length increment distribution and (b) grain size distribution in the "long transverse" direction in the long transverse/short plane (Fig. 2).

thesis, Ecole Nationale Supérieure des Mines de Saint-Etienne (2011)
7. Ben Ali, N., Estevez, R., Tanguy, D.: Heterogeneity of grain boundaries in 5xxx and 7xxx aluminum alloys and its influence on intergranular toughness. Eng. Frac. Mech. **97**, 1–11 (2013)
8. Ben Ali, N., Tanguy, D., Estevez, R.: Effects of microstructure on hydrogen-induced cracking in aluminum alloys. Scripta Mater. **65**, 210–213 (2011)
9. Bendo, A., Matsuda, K., Lee, S., Nishimura, K., Nunomura, N., Toda, H., Yamaguchi, M., Tsuru, T., Hirayama, K., Shimizu, K., Gao, H., Ebihara, K., Itakura, M., Yoshida, T., Murakami, S.: Atomic scale haadf-stem study of η' and η_1 phases in peak-aged AlZnMg alloys. J. Mater. Sci. **53**, 4598–4611 (2018)
10. Bertsch, K., Wang, S., Nagao, A., Robertson, I.: Hydrogen-induced compatibility constraints across grain boundaries drive intergranular failure of Ni. Mat. Sci. Eng. A **760**, 58–67 (2019)
11. Bond, G., Robertson, I., Birnbaum, H.: On the determination of the hydrogen fugacity in an environmental cell tem facility. scripta metall. **20**, 653–658 (1986)
12. Christodoulou, L., Flower, H.: Hydrogen embritlement and trapping in Al-6%-Zn-3%-Mg. Acta Metallurgica **28**, 481–487 (1980)
13. Deng, Y., Barnoush, A.: Hydrogen embrittlement revealed via novel in situ fracture experiments using notched micro-cantilever specimens. acta mater. **142**, 236–247 (2018)
14. Du, J.P., Geng, W.T., Arakawa, K., Li, J., Ogata, S.: Hydrogen-enhanced vacancy diffusion in metals. J. Phys. Chem. Lett. **11**, 70157020 (2020)
15. Du, Y.A., Rogal, J., Drautz, R.: Diffusion of hydrogen within idealized grains of bcc Fe: A kinetic Monte Carlo study. Phys. Rev. B **86**, 174110 (2012)
16. Dumont, M., Lefebvre, W., Doisneau-Cottignies, B., Deschamps, A.: Characterisation of the composition and volume fraction of η' and η precipitates in an AlZnMg alloy by a combination of atom probe, small-angle X-ray scattering and transmission electron microscopy. acta mater. **53**, 2881–2892 (2005)
17. Flanagan, W.F.: What do we understand about stress corrosion cracking in aqueous environments? In: T. Magnin (ed.) Corrosion-Deformation Interactions, CDI '96, pp. 2–11. The Institute of Materials (1997)
18. Flanagan, W.F., Wang, M., Zhu, M., Lichter, B.D.: Authorsŕeply. Metall. Mater. Trans. A **27A**, 820–821 (1996)
19. Gangloff, R.P.: Hydrogen assisted cracking of high strength alloys. In: I. Milne, R.O. Ritchie, B. Karihaloo (eds.) Comprehensive structural integrity, vol. 6, p. 31. Elsevier Science New York, NY (2003)
20. Gangloff, R.P., Somerday, B.P. (eds.): Gaseous Hydrogen Embrittlement of Materials in Energy Technologies. Woodhead, Cambridge, UK (2012)
21. Girardin, G., Huvier, C., Delafosse, D., Feaugas, X.: Correlation between dislocation organization and slip bands: TEM and AFM investigations in hydrogen-containing nickel and nickelchromium. acta mater. **91**, 141–151 (2015)
22. Gjønnes, J., Simensen, C.H.R.: An electron microscope investigation of the microstructure in an aluminium-zinc-magnesium alloy. acta metall. **18**, 881–890 (1970)
23. Gupta, R.K., Deschamps, A., Cavanaugh, M.K., Lynch, S.P., Birbilis, N.: Relating the early evolution of microstructure with the electrochemical response and mechanical performance of a Cu-rich and Cu-lean 7XXX aluminum alloy. J. Elec. Soc. **159**, C492–C502 (2012)
24. Holroyd, N.J.H.: Environment-induced cracking of high strength aluminium alloys. In: R.P. Gangloff, M.B. Ives (eds.) EICM Proceedings, p. 311. Houston Tx: NACE (1990)
25. Holroyd, N.J.H., Burnett, T.L., Seifi, M., Lewandowski, J.J.: Improved understanding of environment-induced cracking (EIC) of sensitized 5XXX series aluminium alloys. Mat. Sci. ENg. A **682**, 613–621 (2017)
26. Holroyd, N.J.H., Scamans, G.M.: Crack propagation during sustained-load cracking of Al-Zn-Mg-Cu aluminum alloys exposed to moist air or distilled water. Metallurgical and Materials Transactions A **42A**, 3979–3998 (2011)
27. Ilin, D.N., Saintier, N., Olive, J.M., Abgrall, R., Aubert, I.: Simulation of hydrogen diffusion affected by stress-strain heterogeneity in polycrystalline stainless steel. International Journal of Hydrogen Energy **39**, 2418–2422 (2014)
28. Ismer, L., Park, M.S., Janotti, A., Van de Walle, C.G.: Interactions between hydrogen impurities and vacancies in Mg and Al: A comparative analysis based on density functional theory. Phys. Rev. B **80**, 184110 (2009)
29. Knight, S., Pohl, K., Holroyd, N., Birbilis, N., Rometsch, P., Muddle, B., Goswami, R., Lynch, S.: Some effects of alloy composition on stress corrosion cracking in AlZnMgCu alloys. Corrosion Science **98**, 50–62 (2015)
30. Lervik, A., Thronsen, E., Friis, J., Marioara, C.D., Wenner, S., Bendo, A., Matsuda, K., Holmestad, R., Andersen, S.J.: Atomic structure of solute clusters in AlZnMg alloys. acta materialia **205**, 116574 (2021)
31. Li, S., Li, Y., Lo, Y.C., et al.: The interaction of dislocations and hydrogen-vacancy complexes and its importance for deformation-induced proto nano-voids formation in α-fe. International Journal of Plasticity **74**, 175–191 (2015)
32. Lozano-Perez, S., Dohr, J., Meisnar, M., Kruska, K.: SCC in PWRs: Learning from a Bottom-Up Approach. Metall. Mater. Trans. E **1A**, 194 (2014)
33. Lynch, S.: Discussion of some recent literature on hydrogen-embrittlement mechanisms: adressing common misunderstandings. Corros. Rev. **37**, 377–395 (2019)
34. Magnin, T. (ed.): Corrosion-Deformation Interactions, CDI '96. The Institute of Materials (1997)
35. Magnin, T., Chambreuil, A., Bayle, B.: The corrosion-enhanced plasticity model for stress corrosion cracking in ductile fcc alloys. Acta Materialia **44**(4), 1457 (1996)
36. Malitckii, E., Yagodzinskyy, Y., Hänninen, H.: Hydrogen uptake from plasma and its effect on EUROFER 97 and

ODS-EUROFER steels at elevated temperatures. Fusion Engineering and Design **98-99**, 2025–2029 (2015)
37. McMurtrey, M., Cui, B., Robertson, I., Farkas, D., Was, G.: Mechanism of dislocation channel-induced irradiation assisted stress corrosion crack initiation in austenitic stainless steel. Current Opinion in Solid State and Materials Science **19**, 305–314 (2015)
38. Mütschele, T., Kirchheim, R.: Segregation and diffusion of hydrogen in grain boundaries of palladium. Scripta Metallurgica **21**, 135 (1987)
39. Nagao, A., Dadfarnia, M., Somerday, B.P., Sofronis, P., Ritchie, R.O.: Hydrogen-enhanced-plasticity mediated decohesion for hydrogen-induced intergranular and "quasi-cleavage" fracture of lath martensitic steels. J. Mech. Phys. Solids **112**, 403–430 (2018)
40. Nazarov, R., Hickel, T., Neugebauer, J.: Ab initio study of H-vacancy interactions in fcc metals: Implications for the formation of superabundant vacancies. Phys. Rev. B **89**, 144108 (2014)
41. Robertson, I.M., Sofronis, P., Nagao, A., Martin, M., Wang, S., Gross, D., Nygren, K.: Hydrogen embrittlement understood. Metallurgical and materials transaction A **46A**, 2323–2341 (2015)
42. Sauzay, M., Ould Moussa, M.: Prediction of grain boundary stress fields and microcrack initiation induced by slip band impingement. Int. J. Fract. **184**, 215–240 (2013)
43. Scamans, G.M., Alani, R., Swann, P.R.: Pre-exposure embrittlement and stress corrosion failure in AlZnMg alloys. Corros. Sci. **16**, 443–459 (1976)
44. Scully, J.R., Young, J.G.A., Smith, S.W.: Gaseous Hydrogen Embrittlement of Materials in Energy Technologies, vol. 1, chap. Hydrogen Embrittlement of Al and Al-Based Alloys, pp. 707–768. Woodhead, Cambridge, UK (2012)
45. Shen, X.J., Connétable, D., Andrieu, E., Tanguy, D.: Segregation of hydrogen and vacancies at the $\sigma5(210)[001]$ symmetric tilt grain boundary in Ni and influence on cohesion. Modelling Simul. Mater. Sci. Eng **29**, 055004 (2021)
46. Shimizu, K., Toda, H., Uesugi, K., Takeuchi, A.: Local deformation and fracture behavior of high-strength aluminum alloys under hydrogen influence. metall. mat. trans. A **51**, 1–19 (2020)
47. Sun, Y., Peng, Q., Lu, G.: Quantum mechanical modeling of hydrogen assisted cracking in aluminum. Phys. Rev. B **88**, 104109 (2013)
48. Tada, H., Paris, P.C., Irwin, G.R.: The stress analysis of cracks handbook. ASME Press, New York (2000)
49. Tanguy, D.: Cohesive stress heterogeneities and the transition from intrinsic ductility to brittleness. Phys. Rev. B **96**, 174115 (2017)
50. Tanguy, D., Delafosse, D., Razafindrazaka, M.: Plasticity localization ahead of a crack tip modeled by 2D discrete dislocation dynamics. Phil. Mag. **90**, 1415–1434 (2010)
51. Tehranchi, A., Curtin, W.A.: Atomistic study of hydrogen embrittlement of grain boundaries in nickel: I. fracture. J. Mech. Phys. Solids **101**, 150–165 (2017)
52. Tehranchi, A., Zhou, X., Curtin, W.A.: A decohesion pathway for hydrogen embrittlement in nickel: Mechanism and quantitative prediction. acta mater. **185**, 98–109 (2020)
53. Valle, V., Hedan, S., Cosenza, P., Fauchille, A., Berdjane, M.: Digital image correlation development for the study of materials including multiple crossing cracks. Exp. Mech. **55**, 379–391 (2015)
54. Van der Ven, A., Ceder, G.: The thermodynamics of decohesion. acta mater. **52**, 1223–1235 (2004)
55. Wan, D., Deng, Y., Barnoush, A.: Hydrogen embrittlement effect observed by in-situ hydrogen plasma charging on a ferritic alloy. Scripta. Mater. **151**, 24–27 (2018)
56. Wang, Y., Connétable, D., Tanguy, D.: Hydrogen influence on diffusion in nickel from first-principles calculations. Phys. Rev. B **91**, 094106 (2015)
57. Wang, Y., Connétable, D., Tanguy, D.: Site stability and pipe diffusion of hydrogen under localised shear in aluminium. Phil. Mag. **99**, 1184–1205 (2019)
58. Wunderlich, W., Gudladtz, H.J.: TEM studies of grain boundaries in cyclically deformed alznmg bicrystals. acta metall. mater. **40**, 2123–2129 (1992)
59. Xie, D., Li, S., Li, M., Wang, Z., Gumbsch, P., Sun, J., Ma, E., Li, J., Shan, Z.: Hydrogenated vacancies lock dislocations in aluminium. nat. comm. **7**, 13341 (2016)
60. Young, G.A., Scully, J.R.: Hydrogen production, absorption and transport during environment assisted cracking of an Al-Zn-Mg-(Cu) alloy in humid air. In: International Conference on Hydrogen Effects on Material Behavior and Corrosion Deformation Interactions, pp. 22–26. Moran, WY (2002)
61. Zamora, R.J., Nair, A.K., Hennig, R.G., Warner, D.H.: Ab initio prediction of environmental embrittlement at a crack tip in aluminum. Phys. Rev. B **86**, 060101(R) (2012)
62. Zhou, X., Mousseau, N., Song, J.: Is hydrogen diffusion along grain boundaries fast or slow? atomistic origin and mechanistic modeling. Phys. Rev. Lett. **122**, 215501 (2019)